Airborne measurements of atmospheric methane column abundance using a pulsed integrated-path differential absorption lidar

Haris Riris,[1,*] Kenji Numata,[2] Steve Li,[3] Stewart Wu,[3] Anand Ramanathan,[4]
Martha Dawsey,[1] Jianping Mao,[5] Randolph Kawa,[1] and James B. Abshire[1]

[1]NASA, Goddard Space Flight Center, Science and Exploration Directorate, Greenbelt, Maryland 20771, USA

[2]Department of Astronomy, University of Maryland, College Park, Maryland 20742, USA

[3]NASA, Goddard Space Flight Center, Lasers and Electro-Optics Branch, Greenbelt, Maryland 20771, USA

[4]Oak Ridge Associated Universities, P.O. Box 117, Oak Ridge, Tennessee 37831-0117, USA

[5]Goddard Earth Sciences Technology and Research, Goddard Space Flight Center,
8800 Greenbelt Rd., Greenbelt, Maryland 20771, USA

*Corresponding author: haris.riris@nasa.gov

Received 24 August 2012; accepted 11 October 2012;
posted 25 October 2012 (Doc. ID 174901); published 30 November 2012

We report airborne measurements of the column abundance of atmospheric methane made over an altitude range of 3–11 km using a direct detection integrated-path differential-absorption lidar with a pulsed laser emitting at 1651 nm. The laser transmitter was a tunable, seeded optical parametric amplifier pumped by a Nd:YAG laser, and the receiver used a photomultiplier detector and photon-counting electronics. The results follow the expected changes with aircraft altitude, and the measured line shapes and optical depths show good agreement with theoretical calculations. © 2012 Optical Society of America

OCIS codes: 010.0280, 280.1910, 280.3640, 300.1030.

1. Introduction

The last report by the Intergovernmental Panel on Climate Change [1] attributes the increase of the atmospheric concentrations of greenhouse gases above their preindustrial levels to the burning of fossil fuels and other anthropogenic sources. As the concentration of greenhouse gases steadily increases, the subsequent radiative forcing will likely have a significant impact on Earth's climate. Presently our knowledge and understanding of the important processes controlling greenhouse gas concentrations is incomplete. Current observations of greenhouse gases are mostly from *in situ* (surface and tower) sites, airborne, and space-based measurements from passive spectrometers. Initial space measurements of methane and other greenhouse gases came from SCIAMACHY on European Space Agency's (ESA's) environmental satellite (ENVISAT) mission [2–4], the infrared atmospheric sounding interferometer (IASI) on the Centre National d'Etudes Spatiales's (CNES) MetOp satellite [5,6], and NASA's atmospheric infrared sounder (AIRS) on that agency's Aqua Mission [7,8]. Additional space measurements are now available from Japan Aerospace Exploration Agency or Japan Space Exploration Agency's (JAXA's) greenhouse gases observing satellite (GOSAT) mission, which was launched in 2009 [9–12]. All four

1559-128X/12/348296-10$15.00/0

instruments are passive spectrometers, and their observations are limited. Measurements using surface-reflected sunlight by GOSAT and SCIAMACHY are limited to the sunlit areas of earth, and their data products are significantly affected by atmospheric scattering and the presence of clouds [13,14]; measurements in thermal infrared by AIRS and IASI have a measurement weighting function peaked in the mid-troposphere [15] and are not sensitive to the sources and sinks of greenhouse gases at the surface but are very sensitive to atmospheric temperature changes.

Although CO_2 is currently the largest carbon-based greenhouse gas, methane is also important because its radiative forcing is approximately 23 times larger per molecule than that of CO_2 [1]. The methane mixing ratio is presently at ~1.8 parts per million by volume and has been increasing along with CO_2 [15,16]. Natural sources of methane include wetlands, wild fires, and termites [17]. Anthropogenic sources of methane include fossil fuel production, rice farming, livestock, and landfills. Important sinks for methane include oxidation by hydroxyl radicals in the atmosphere and oxidation by nonsaturated soils.

Large amounts of methane are also contained in the continental shelf in the form of methane hydrates [18]. The large reservoirs of carbon trapped in the permafrost regions of northern Siberia, North America, and Europe are a major concern. As global temperatures rise and the permafrost thaws, some of the carbon will be converted to methane and will be released into the atmosphere, adversely affecting the climate [19,20]. Better knowledge of the methane distribution and understanding of the sources and sinks is imperative for a better assessment of its impact on global change [21–23].

The U.S. National Research Council also recognized the importance of measuring methane, and its last Decadal Survey for Earth Science [24] recommended that NASA implement an active (laser-based) space mission to measure CO_2 emissions called active sensing of CO2 emissions over nights, days, and seasons (ASCENDS) and added the following statement: "Ideally, to close the carbon budget, methane should also be addressed, but the required technology is not now obvious. If appropriate and cost-effective methane technology becomes available, methane capability should be added." The ASCENDS working group is in the process of defining measurement requirements for the mission [25]. Although the final ASCENDS requirements have not yet been released, its launch date has been deferred by budgetary constraints.

The French CNES in collaboration with the German Aerospace Centre is developing a small lidar-based methane mission called the Methane Remote Sensing Lidar Mission (MERLIN) scheduled for launch in 2016 [26–28]. MERLIN targets an 8 part per billion volume (ppbv) relative random error in the methane column abundance with a 50 km horizontal resolution to be scientifically useful.

Measuring methane and its isotopes in planetary atmospheres can also aid in understanding planetary processes and in the search for extraterrestrial life. Habitable environments are believed to have existed previously on Mars and could potentially persist today. The presence and distribution of methane and other gases of possible biogenic origin may provide evidence for subsurface biology and help better locate regions for more intensive study. Recent planetary missions and ground-based observations have provided evidence of reservoirs of methane and water on Mars [29–33] that could potentially harbor life. The observations also suggested large seasonal and spatial variations of methane concentrations.

The Mars trace gas orbiter (TGO) is an ESA mission currently under development that is scheduled to launch in 2016 [34]. It will make very sensitive measurements of a broad suite of atmospheric trace gases and characterize the spatial and temporal variability of methane and other key species with passive spectrometers. In the future, a laser-based spectrometer (a lidar) can provide much better spatial resolution to localize areas of high methane concentrations (e.g., plumes or vents) discovered by TGO and map the global distribution of these gases over day and night and at all latitudes. The requirements for an active methane instrument on Mars are likely to require 1 ppb or below detection sensitivity over a relatively small area (a few tens of square kilometers) in order to localize methane sources. For these applications, measuring methane is a detection problem—namely, detecting the presence of a small signal against a small background.

At Goddard space flight center (GSFC) we have developed lidar technology based on optical parametric amplifiers (OPAs) that can be used to measure methane remotely from an orbiting platform. The transmitter technology is applicable to both Earth and planetary atmospheres but requires different detectors. Using this technology we have demonstrated measurements of methane, carbon monoxide and dioxide, and water vapor on the ground [35,36], and in the summer of 2011 we demonstrated methane measurements from an airborne platform in California at altitudes from 3 to 11 km. The latter measurements are the subject of this work.

2. Methane Spectroscopy

Methane has absorptions in most of the near- and mid-IR spectral range. The strongest bands are at 1.65, 2.2, 3.3, and 7.8 μm. The band at 3.3 μm is ideal for making high-sensitivity measurements of methane in low-pressure planetary atmospheres, such as that of Mars. The average surface pressure on Mars is ~6 mbar, which results in negligible pressure broadening (typically <30 MHz full width at half maximum) so the absorption lines are essentially Doppler-broadened. A laser spectrometer with sufficient signal-to-noise ratio (SNR) and high spectral resolution would be an ideal candidate for measuring methane from a Mars orbit.

In the Earth's atmosphere the methane lines in the 3.3 μm spectral region may be suitable for pipeline leak detection and other similar low-altitude applications [37–40] that use relatively short paths (typically <1 km) and for *in situ* detection [41–43]. However, most methane lines near 3.3 μm are too strong for space use because they would completely absorb the laser radiation before it reached the ground. There is also significant interference from the wings of adjacent water vapor and other absorption lines in this spectral region. Water vapor is a particular issue because it is highly variable in the Earth's atmosphere and would make accurate measurements of methane from space at 3.3 μm very difficult.

The overtone lines of methane at 1.65 μm, however, are well suited for remote sensing of atmospheric methane in the Earth's atmosphere. The lines are almost two orders of magnitude weaker than those at 3.3 μm, but they are relatively free of interference from other atmospheric species. For example, Fig. 1 shows the two-way transmittance through a U.S. standard atmosphere from an orbit of 400 km for a methane line at 1650.95 nm calculated using the HITRAN 2008 database [44]. This candidate methane line is strong enough to be used for lidar observations and has very little interference from other species.

3. Laser Approach and Technology

We have developed a direct-detection lidar to measure column methane abundance using the integrated-path differential absorption (IPDA) technique. It uses a tunable pulsed laser, whose spectral emission can be rapidly tuned across a selected methane absorption line, and a time-resolved receiver using a sensitive detector to detect the reflected laser energy.

We chose a laser based on optical parametric generation (OPG) to generate tunable radiation at 1.65 and 3.3 μm. In OPG, a photon of an incident laser pulse (pump) is divided into two photons, a signal and an idler, by a nonlinear optical crystal. The wavelengths of the signal and the idler must that satisfy the energy and phase-matching conditions in the crystal. An OPA is a seeded version of OPG.

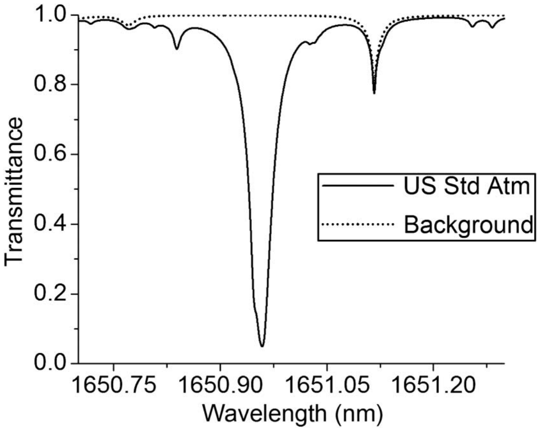

Fig. 1. Two-way atmospheric transmittance of methane at 1651 nm from a 400 km orbit for a U.S. standard atmosphere. The dotted curve is the two-way atmospheric transmittance without methane (background).

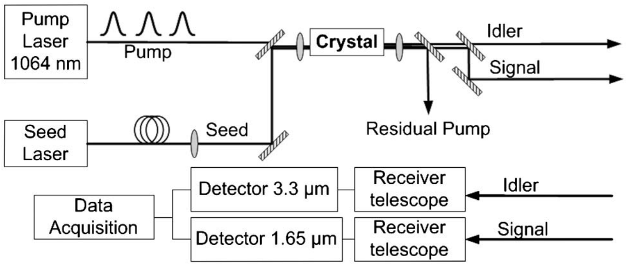

Fig. 2. Block diagram of the OPA-based IPDA lidar.

A simplified block diagram of our OPA-based lidar is shown in Fig. 2. A nonlinear periodically poled lithium niobate (PPLN) crystal is pumped by a pulsed single-frequency 1064 nm Nd:YAG laser and seeded by a continuous-wave (CW) 1651 nm distributed-feedback (DFB) laser diode. The wavelength of the seed laser can be easily changed by changing the diode laser. We used seed laser diodes at 1578 nm to generate an idler wavelength at 3.3 μm and 1651 nm to amplify the seed wavelength for 1651 nm applications. In principle, any diode laser between 1530 and 1660 nm can be used as a seed in order to target different trace gases in the 1.5–1.65 μm and 3–4 μm range. Diode lasers are small, rugged, and have very desirable spectroscopic characteristics: their side-mode suppression ratio typically exceeds 40 dB, they tune smoothly over a few nanometers, their wavelength can be tightly controlled via the temperature and current to the diode, and the instantaneous linewidth can be less than 1 MHz. They also can also be frequency stabilized using external reference cells [45].

The two beams (seed and pump) are coaligned and focused through the PPLN crystal. The temperature of the crystal can be tuned between 70°C and 170°C to optimize the phase matching at the target wavelength. The output beam is separated into three wavelength paths using dichroic mirrors. Depending on the application (Earth or Mars), the signal, the idler, or both can be used for trace gas detection through an absorption cell or in an open path. For open path measurements the returns at 1651 nm and 3.3 μm are collected by commercial telescopes and detected by InGaAs and HgCdZnTe detectors, respectively. The return signals are averaged by a boxcar averager and digitized by a computer for processing and display. A description of the different OPA systems we have used for ground-based measurements was given by Numata *et al.* [35]. In this paper, we discuss using the OPA-based transmitter operating at 1651 nm to measure methane column abundance from an aircraft.

4. Airborne Lidar

For our airborne demonstration we used an enhancement of the IPDA technique [46], using a sequence of discrete laser pulses that were repetitively stepped in wavelength across the line. Ideally only two wavelengths are needed for an IPDA lidar to determine the line's transmission and determine the path-integrated atmospheric column density. In practice, however, using more wavelengths and measuring the line shape is quite valuable. This additional data allows solving for variable instrumental and systematic errors, such as etalon fringes with various periods and baseline drifts. Our airborne methane lidar used 20 wavelengths distributed evenly across the line.

The methane lidar measures the total transmittance, $\tau(\nu)$, of the emitted laser energy, E_0, through the atmospheric column (from the aircraft to the ground and back). The received energy, E, can be written as

$$E = E_0 \eta \frac{A}{R^2} \frac{\beta}{\pi} \tau^2(\nu), \qquad (1)$$

where η is the receiver efficiency, β is the ground surface reflectivity, A is the collecting area of the receiver, R is the range to the surface, and ν is the laser frequency. The total transmittance over the atmospheric column is an integral over all atmospheric layers, dr, between the aircraft and the ground:

$$\tau(\nu) = e^{-2\int_0^R \sigma(\nu,T,P)N(r)\mathrm{d}r}, \qquad (2)$$

where $\sigma(\nu, T, P)$ is the molecular absorption cross section for a given atmospheric layer and $N(r)$ is the corresponding number density in each atmospheric layer.

The absorption cross section is a function of the temperature, T, and pressure, P, at each atmospheric layer, and the natural logarithm of the transmittance, $\ln(\tau(\nu))$, is usually referred to as the optical depth (OD). The differential optical depth (DOD), or the OD "on" and "off" the absorption at λ_{on} and λ_{off}, is a useful quantity because, to the first order, it increases linearly with the number density. As stated above, an IPDA lidar may be designed to use two wavelengths ("on" and "off" the absorption, λ_{on} and λ_{off}) or multiple wavelengths to trace the entire line shape. The OD and DOD changes at λ_{on} and λ_{off} can be used to assess the SNR and performance of an IPDA lidar [47–50].

A. Laser Operation and Data Recorder

For airborne operations the ground-based methane instrument was modified to fit into the NASA DC-8. A more robust optomechanical design was implemented to prevent misalignment in the aircraft environment. A block diagram of the airborne instrument is shown in Fig. 3. The pump laser is a passively Q-switched Nd:YAG nonplanar ring oscillator made by Innolight Inc. that emits single-frequency output at 1064.5 nm. It has 3 ns pulse width and maximum energy of 60 μJ per pulse at a 6.3 kHz repetition rate. The laser is operating in a single mode, and its optical linewidth is transform limited (~133 MHz). A beam splitter directs a small portion of the pump laser onto a high-speed photodiode (EO Technologies ET-3000) that provides a trigger for the data acquisition sequence. The OPA is seeded by a CW 1651 nm commercial DFB laser made by NEL America (part no. NLK1U5FAAA). The two beams (pump and seed) are coaligned and focused through the OPA crystal. The OPA crystal is a 50 mm long, 1 mm thick, MgO-doped PPLN with a 31.0 μm grating. The end surfaces of the crystal are angled at 5° and antireflective coated at the pump, the signal, and the idler wavelengths in order to minimize optical feedback and etalon fringes. The temperature of the crystal is controlled by an oven and temperature controller. The output beams from the OPA are collimated and separated into three wavelength paths using dichroic mirrors (not shown in Fig. 3 for simplicity). The idler and residual pump wavelengths are not used in the airborne experiment. The signal beam from the OPA is sent through a beam expander to reduce its divergence to 250–300 μrad and then directed to the ground through the nadir port of the aircraft.

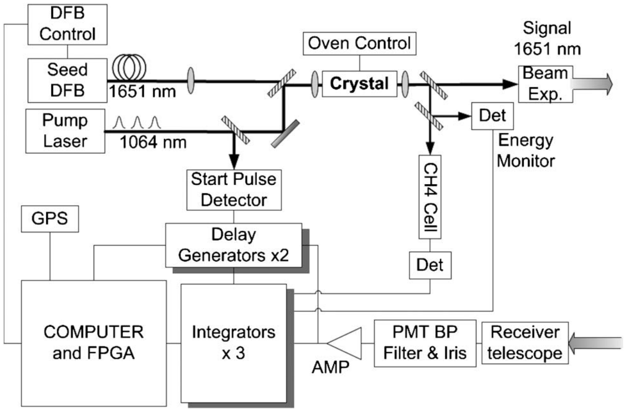

Fig. 3. Block diagram of the airborne lidar. The idler and residual pump beams were not used and are not shown in the diagram.

A beam splitter directs part of the outgoing 1651 nm beam through a short (8 cm) CH_4 reference cell at 370 Torr that is used for wavelength calibration. Another part of the outgoing beam is sent on to an InGaAs detector (Thorlabs DET10C) that serves as an energy monitor. The output signal from the cell and the energy monitor are integrated by gated integrators (Signal Recovery Model 4121B) and then digitized by an analog-to-digital converter (ADC).

The reflected ground echoes are collected by a commercial 20 cm diameter receiver telescope (Vixen VC200L) and are coupled into an AR-coated 600 μm core multimode fiber (Fiberguide CB18167). The receiver field of view (FOV) is determined by the telescope effective focal length (2 m), the receiver fiber core size, and its numerical aperture. In our case the FOV is 300 μrad. The receiver fiber output is collimated and directed through a 0.8 nm (FWHM) bandpass filter (Barr Associates), an iris for signal attenuation, and then onto a photon-counting detector [Hamamatsu photomultiplier tube (PMT) Part No H10330A-75]. The quantum efficiency of the PMT at 1651 nm is approximately 1%. A high-speed amplifier amplifies the PMT signal for data acquisition. A computer with a field-programmable gate array (FPGA; National Instruments 7831-R), along with

Table 1. Flight Lidar Parameters

Parameter	Value
Seed wavelength	1650.9 nm
Pump wavelength	1064 nm
Laser pulse rate	~6.3 kHz
Laser pulse width	3 ns
Laser pump energy	60 μJ
Seed power	15 mW
OPA energy	10 μJ
Laser divergence	~300 μrad
Receiver diameter	20 cm
Receiver field of view	300 μrad
Receiver bandpass	800 pm (FWHM)
Scan rate	~250 Hz
Averaging period	1 s
Detector efficiency	~1%

two delay generators (Stanford Research Systems DG645), provide the necessary timing signals, wavelength scan waveforms, and appropriate delays for the data acquisition system. The major parameters of the airborne system are summarized in Table 1.

The lidar receiver electronics had to accommodate the various flight conditions (changing altitude and topography) and the photon-counting detector input.

The flight data acquisition system uses the PMT in analog mode. A gated integrator (Signal Recovery Model 4121B) integrates the return pulses and produces a time series of the transmittance through the atmospheric column. The seed wavelength was step-scanned over the absorption line using 20 evenly spaced wavelengths. The gate window for the return pulses was set to 20 ns, and its delay was set by the FPGA. The delay was adjusted during flight by measuring the time of flight (TOF) between the start and the echo pulse. All the data was time tagged by a GPS unit that also provided position information.

5. Aircraft and Flights

The airborne flights were performed on NASA's DC-8 aircraft, which is based at the Dryden Airborne Operations Facility (DAOF) in Palmdale, California. Just prior to our methane flights the NASA ASCENDS program had completed a series of flights to measure column CO_2 using the same aircraft. We were able to share some of the GSFC personnel and equipment to minimize cost for these experiments. We chose to overfly California's Central Valley because of its proximity to Palmdale and for its possible methane sources (livestock feedlots, oil fields, and natural-gas storage sites). The flight instrument was integrated onto the airplane in early August 2011. The instrument complement included the GSFC CO_2 Sounder GPS; a Picarro *in situ* analyzer that measures methane, carbon dioxide, and water vapor using wavelength-scanned cavity ring down spectroscopy [32]; and other ancillary instruments (Fig. 4).

The methane lidar flew three flights over California's Central Valley on August 23, 24, and 25, 2011. All the flights traversed similar paths and were routed away from high traffic and adjacent military operations areas. The flight paths were anchored near Bakersfield, California, at the southern end and near Coalinga at the northern end. Each flight lasted about 2.5 h and consisted of several segments at constant altitudes at approximately 3, 4.8, 6.2, 7.9, 9.5, and 11.1 km (10, 15, 20, 25, 30, and 36 thousand feet). The exact altitudes varied slightly with each flight. The flight paths and altitude profiles for the three flights are shown in Figs. 5 and 6 respectively. The order of the flight altitude segments was reversed for the August 25 flight, and the flight path deviated slightly to the west compared to the two previous flights. The terrain in the Central Valley varies between dry desert and cultivated areas with a gently changing topography.

6. Airborne Measurements and Results

The integrated, normalized return pulse energies from the lidar as a function of wavelength represent the transmittance through the atmospheric column. As a first step in analyzing our measurements, we compare our obtained transmittance profile to the predicted transmittance profile. The theoretical transmittance profiles are generated by calculating the transmittance for each layer as a function of range, pressure, temperature, water vapor pressure, and of course, the mixing ratio of methane and other atmospheric constituents. The calculations use a line-by-line radiative transfer model [50] and the

Fig. 4. (Color online) (left) NASA's DC-8 aircraft at DAOF prior to a methane flight and (right) the methane lidar in the aircraft. The lidar used two aircraft racks and a transceiver.

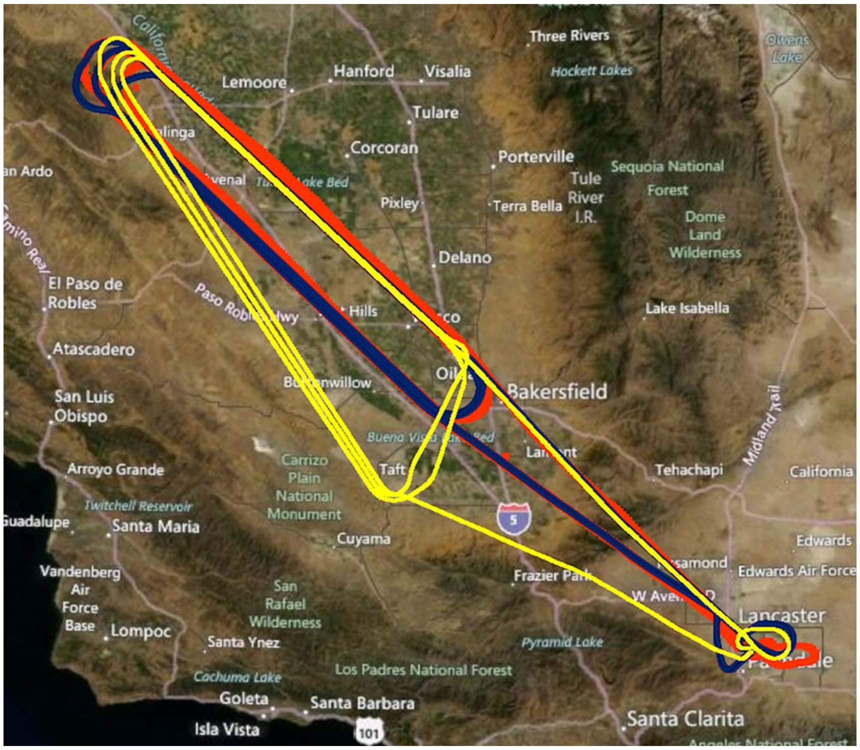

Fig. 5. (Color online) Flight paths in Central Valley, California (red: August 23 flight; blue: August 24 flight; yellow: August 25 flight).

HITRAN 2008 database. The range to the ground is determined by the TOF between the start pulse and the echo pulse using the FPGA. The accuracy of the range measurement was approximately 2 m, comparable to what was obtained by Amediek *et al.* [51] with a similar lidar instrument. Ancillary meteorological data is also needed to calculate the state of the atmosphere and implement a retrieval algorithm.

Most of the additional meteorological data came from the aircraft data acquisition system, which measures pressure, temperature, GPS location, dew point, wind speed, and many other parameters of interest. Our flight segments were relatively close to each other, and the airplane meteorological data was adequate in providing data for the atmospheric layers above 3 km. However, we needed additional data for the layers below 3 km. The meteorological data during the ascent and descent to Palmdale were not useful because they were not taken in the vicinity of our main flight path. We obtained the additional meteorological data for our flights from the Global Modeling and Assimilation Office (GMAO) [52]. The GMAO develops models and assimilates observations from satellites and ground systems to generate meteorological products that are used for various NASA missions. Using these data we calculated the theoretical spectra of the expected atmospheric transmittance, OD, and DOD as a function of altitude, an example of which is illustrated in Fig. 7.

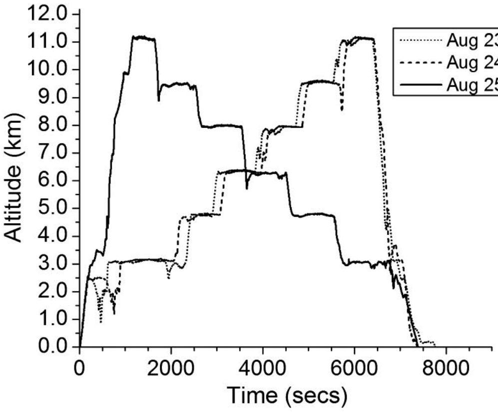

Fig. 6. Flight altitude profiles for the three methane lidar flights in 2011.

We processed the data by first subtracting a constant offset (~2–4% of the integrated pulse energy) arising from the integrator electronics. The offset-corrected integrated pulse energies were then averaged over 20 s and then normalized by the mean off-peak (pulses 1–3 and 18–20) pulse energy to give the transmittance. We then used our wavelength reference, transmission through the onboard methane cell, to calibrate our wavelength scan, thus giving the measured transmittance versus wavelength profile shown in Fig. 8. This measured transmittance was found to be in good agreement with the theoretical prediction.

In order to perform methane concentration retrievals, we need to fit the data to a model function with a free parameter for the methane concentration. We use the theoretical curve but allow for a scale factor of the OD to vary the transmittance in a way that reflects a change in the methane concentration. Thus, for every 20 s averaged transmittance profile, we obtain an optimum scale factor along with a modified model profile that corresponds to the best fit. We

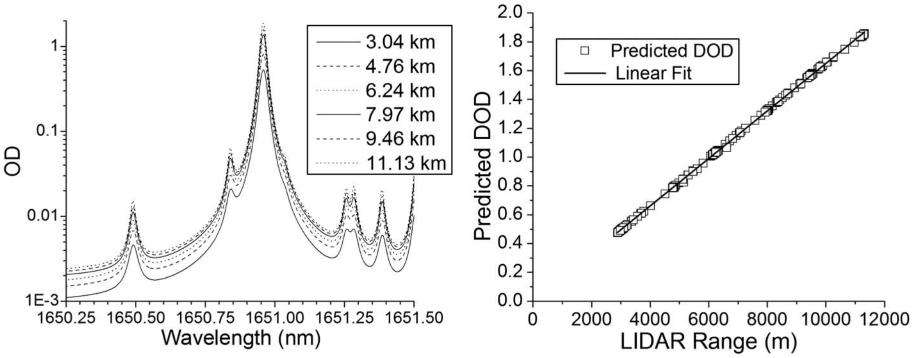

Fig. 7. Examples of calculated OD examples (log scale) as a function of wavelength for different flight altitudes, and calculated DOD as a function of altitude for the August 25 flight using GMAO data and HITRAN 2008.

use this modified profile to obtain the DOD, or the difference in OD between the peak absorption ("on" wavelength) and 100 pm away from the peak ("off" wavelength).

Figure 9 shows the retrieved DOD as a function of time along with the measured lidar range. As expected, the measured DOD increases with flight altitude. In addition, at each flight altitude change when the plane is turning the DOD increases because of the longer (slant) optical path. Figure 10 shows a comparison of the measured lidar DOD and the DOD predictions. A linear fit of the measured DOD versus the theoretical DOD prediction shows a slope of 1.036 and a small offset of −0.012. The R^2 value of the fit is 0.994. The standard error in the slope estimate was 0.00045, and the standard deviation of the residuals of the fit was 0.0033.

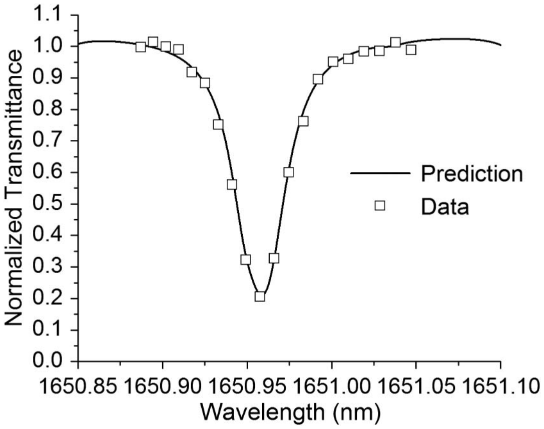

Fig. 8. Retrieved transmittance versus wavelength at a flight altitude of 9.6 km and comparison with the prediction using line-by-line calculations with the HITRAN 2008 database for the August 25 flight. A 20 s averaging period was used.

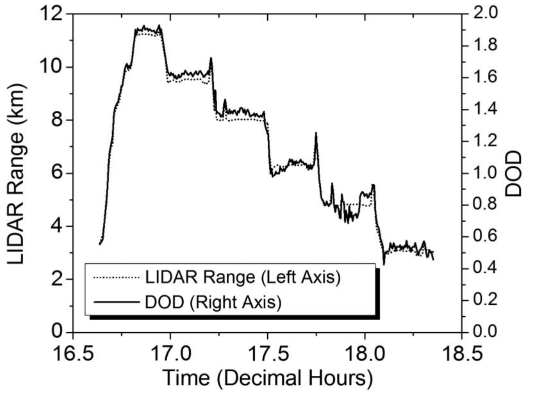

Fig. 9. Measured lidar range and the corresponding DOD versus time for the August 25 flight.

Along with the DOD, the retrievals estimated the methane column mixing ratio. Figure 11 shows the methane mixing ratio for the August 25 flight along with the *in situ* CRDS instrument (Picarro) values as a function of flight time in decimal hours (UTC, coordinated universal time). A 20 s averaging period was used.

7. Discussion

Overall the lidar and the Picarro showed reasonable agreement. The lidar mixing ratio values were noisier and varied more than those of the Picarro. The noise increased at lower altitudes where the methane absorption gets smaller as the range (path length) gets shorter. Some of the sudden changes in the methane mixing ratio later in the flight were due to alignment adjustments of the instrument during flight. We do not expect the lidar and the Picarro to agree perfectly. The *in situ* measurements are

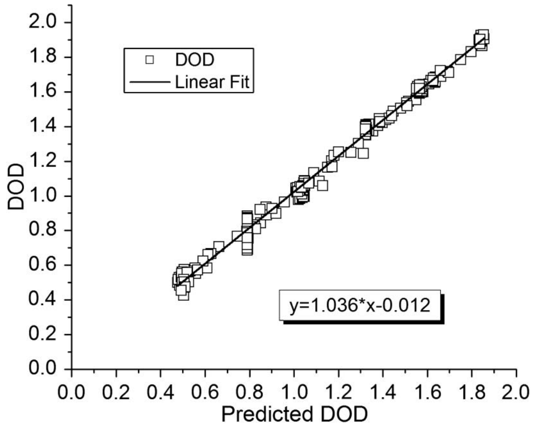

Fig. 10. Measured DOD versus theoretical DOD prediction with a linear fit for the August 25 flight (right). A 20 s averaging period was used.

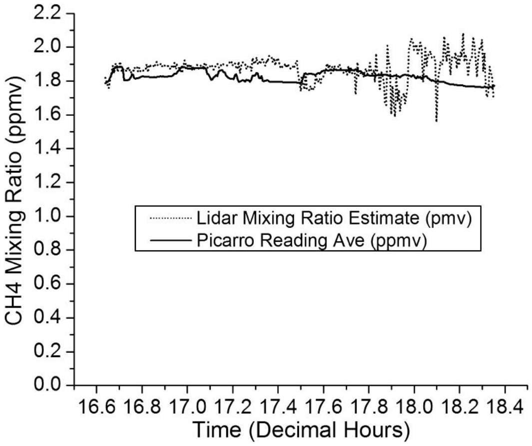

Fig. 11. Comparison of the lidar methane mixing ratio with the *in situ* CRDS instrument (Picarro) values as a function of flight time in decimal hours (UTC) for the August 25 flight. A 20 s averaging period was used.

point measurements taken at a particular flight altitude whereas the methane lidar measures the entire column to the surface.

The lidar measurements were affected by several random and systematic noise sources. The low quantum efficiency of the PMT at 1651 nm and the relatively low power of the laser transmitter produced noisy data. The laser power needs to be increased considerably for a space application. The boresight alignment was also an issue, and we had to check and adjust the receiver alignment during flight. This issue can be mitigated by a more robust optomechanical design. The integrator electronics also introduced a bias that was subtracted from the integrated pulse energies. The bias is calibrated on the ground prior to or after the flights. However, it is possible that it may vary during flight. We are currently trying to substitute our integrator electronics with fast digitizers that will sample the pulse waveform and mitigate this issue. Finally another significant nonrandom noise component that degraded our SNR was etalon fringes in our transmitter. Etalon fringes are unwanted optical interference patterns that arise from multiple weak reflections from each optical surface in the optical path. They are a function of small path-length changes due to optomechnical shifts, temperature, and changes in the index of refraction, and they can limit the detection sensitivity and averaging time of a laser spectrometer [53]. They can manifest themselves as real signals and can introduce biases in the measurement and make retrievals difficult as they change over time. Various signal processing techniques have been suggested for reducing their impact [54–56], but none of these techniques have been completely successful. Our transmitted beam exhibited a large fringe, which was then superimposed on the return pulses. We believe that the fringe is the result of reflections from the crystal or one of the other optical elements in the path (lenses and beam splitters). On the ground system we were able to use the energy monitor signal to remove the effect of the etalon fringe. Unfortunately on the flight system the normalization with the energy monitor actually proved detrimental because the fringes on the receiver and the energy monitor exhibited different phases and free spectral range. The presence of the fringe limited the ability of the fitting algorithm to find a good fit and increased our overall error. We believe that with better optomechanical design and adequate preflight testing we can overcome these problems and improve our results.

8. Summary

We have demonstrated airborne measurements of methane absorption and column abundance using a pulsed direct-detection lidar and the IPDA technique. The lidar operates at the 1650.95 nm methane line, and the laser was stepped-scanned over the absorption with 20 evenly spaced wavelength steps. The return pulses were gated and integrated to produce a transmittance measurement through the atmospheric column. We flew three flights in the Central Valley of California on NASA's DC-8 flying laboratory. All flights consisted of flight segments at stepped altitudes from 3 to11 km. A retrieval algorithm estimated the OD and methane mixing ratio by fitting the experimental data to the theoretical predictions. The fitted line shapes agreed well with those predicted from the line-by-line radiative transfer calculations with the HITRAN 2008 database and the airplane and GMAO meteorological data.

The dominant error source for these flights was etalon fringes in the lidar that added unwanted structure to our line shapes. The low transmitter power and 1% quantum efficiency of the detector were also significant limitations. We are currently in the process of increasing the power of the laser transmitter and the detector sensitivity. With improved stability and higher laser power and detector efficiency, this approach can be used for airborne studies of methane columns for carbon cycle science investigations. Once further laser power scaling and detector improvements are accomplished, a space lidar using this approach should be feasible.

This research was funded by the NASA Astrobiology Technology Instrument Development program. We would like to thank Dr. Michael New for his support throughout the program. We would also like to thank the Earth Science Technology Office (ESTO), and the Instrument Incubation Program, and the Goddard CO_2 Sounder team for their equipment loan and for their assistance.

References

1. Intergovernmental Panel on Climate Change (IPCC), http://www.ipcc.ch/index.htm.
2. P. Bergamaschi, C. Frankenberg, J. F. Meirink, M. C. Krol, F. J. Dentener, T. Wagner, U. Platt, J. O. Kaplan, S. Körner, M. Heimann, E. J. Dlugokencky, and A. De Goede, "Satellite chartography of atmospheric methane from SCIAMACHY on board ENVISAT2. Evaluation based on inverse model simulations," J. Geophys. Res. Atmos. **112**, D02304 (2007).

3. M. Buchwitz, R. De Beek, J. P. Burrows, H. Bovensmann, T. Warneke, J. Notholt, J. F. Meirink, A. P. H. Goede, P. Bergamaschi, S. Körner, M. Heimann, and A. Schulz, "Atmospheric methane and carbon dioxide from SCIAMACHY satellite data: initial comparison with chemistry and transport models," Atmos. Chem. Phys. **5**, 941–962 (2005).
4. C. Frankenberg, J. F. Meirink, P. Bergamaschi, A. P. H. Goede, M. Heimann, S. Körner, U. Platt, M. van Weele, and T. Wagner, "Satellite cartography of atmospheric methane from SCIAMACHY on board ENVISAT: analysis of the years 2003 and 2004," J. Geophys. Res. **111**, D07303 (2006).
5. A. Razavi, C. Clerbaux, C. Wespes, L. Clarisse, D. Hurtmans, S. Payan, C. Camy-Peyret, and P. Coheur, "Characterization of methane retrievals from the IASI space-borne sounder," Atmos. Chem. Phys. **9**, 7889–7899 (2009).
6. T. August, D. Klaes, P. Schlussel, T. Hultberg, M. Crapeau, A. Arriaga, A. O'Carroll, D. Coppens, R. Munro, and X. Calbet, "IASI on Metop-A: operational level 2 retrievals after five years in orbit," J. Quant. Spectrosc. Radiat. Transfer **113**, 1340–1371 (2012).
7. P. F. Coheur, X. Xiong, C. D. Barnet, Q. Zhuang, T. Machida, C. Sweeney, and P. K. Patra, "Mid-upper tropospheric methane in the high Northern Hemisphere: spaceborne observations by AIRS, aircraft measurements, and model simulations," J. Geophys. Res. **115**, D19309 (2010).
8. X. Xiong, C. Barnet, E. Maddy, J. Wei, X. Liu, and T. S. Pagano, "Seven years' observation of mid-upper tropospheric methane from atmospheric infrared sounder," Remote Sens **2**, 2509–2530 (2010).
9. T. Yokota, H. Oguma, I. Morino, A. Higurashi, T. Aoki, and G. Inoue, "Test measurements by a BBM of the nadir-looking SWIR FTS aboard GOSAT to monitor CO_2 column density from space," Proc. SPIE **5652**, 182 (2004).
10. T. Yokota, Y. Yoshida, N. Eguchi, Y. Ota, T. Tanaka, H. Watanabe, and S. Maksyutov, "Global concentrations of CO_2 and CH_4 retrieved from GOSAT: first preliminary results," Sci. Online Lett. Atmos. **5**, 160–163 (2009).
11. I. Morino, O. Uchino, M. Inoue, Y. Yoshida, T. Yokota, P. O. Wennberg, G. C. Toon, D. Wunch, C. M. Roehl, J. Notholt, T. Warneke, J. Messerschmidt, D. W. T. Griffith, N. M. Deutscher, V. Sherlock, B. Connor, J. Robinson, R. Sussmann, and M. Rettinger, "Preliminary validation of column-averaged volume mixing ratios of carbon dioxide and methane retrieved from GOSAT short-wavelength infrared spectra," Atmos. Meas. Tech. **4**, 1061–1076 (2011).
12. Y. Yoshida, O. Yoshifumi, E. Nawo, K. Nobuhiro, N. Koji, T. Ha, M. Isamu, and Y. Tatsuya, "Retrieval algorithm for CO_2 and CH_4 column abundances from short-wavelength infrared spectral observations by the Greenhouse Gases Observing Satellite," Atmos. Meas. Tech. **4**, 717–734 (2011).
13. J. Mao and S. R. Kawa, "Sensitivity studies for space-based measurement of atmospheric total column carbon dioxide by reflected sunlight," Appl. Opt. **43**, 914–927 (2004).
14. I. Aben, O. Hasekamp, and W. Hartmann, "Uncertainties in the space-based measurements of CO_2 columns due to scattering in the Earth's atmosphere," J. Quant. Spectrosc. Radiat. Transfer **104**, 450–459 (2007).
15. E. S. Maddy, C. D. Barnet, M. Goldberg, C. Sweeney, and X. Liu, "CO_2 retrievals from the atmospheric infrared sounder: methodology and validation," J. Geophys. Res. **113**, D11301 (2008).
16. E. J. Dlugokencky, S. Houweling, L. Bruhwiler, K. A. Masarie, P. M. Lang, J. B. Miller, and P. P. Tans, "Atmospheric methane levels off: temporary pause or a new steady state," Geophys. Res. Lett. **30**, 1–4 (2003).
17. E. J. Dlugokencky, L. Bruhwiler, J. W. C. White, L. K. Emmons, P. C. Novelli, S. A. Montzka, K. A. Masarie, P. M. Lang, A. M. Crotwell, J. B. Miller, and L. V. Gatti, "Observational constraints on recent increases in the atmospheric CH_4 burden," Geophys. Res. Lett. **36**, L18803 (2009).
18. K. Kvenvolden, "Methanehydrate: a major reservoir of carbon in the shallow geosphere?," Chem. Geol. **71**, 41–51 (1988).
19. F. Keppler, J. T. G. Hamilton, M. Bra, and T. Roeckmann, "Methane emissions from terrestrial plants under aerobic conditions," Nature **439**, 187–191 (2006).
20. T. R. Christensen, T. Johansson, H. J. Akerman, M. Mastepanov, N. Malmer, T. Friborg, P. Crill, and B. H. Vensson, "Thawing sub-arctic permafrost: effects on vegetation and methane emissions," Geophys. Res. Lett. **31**, L04501 (2004).
21. K. M. W. Anthony, P. Anthony, G. Grosse, and J. Chanton, "Geologic methane seeps along boundaries of Arctic permafrost thaw and melting glaciers," Nat. Geosci. **5**, 419–426 (2012).
22. E. Kort, S. Wofsy, B. Daube, M. Diao, J. Elkins, R. Gao, E. Hintsa, D. Hurst, R. Jimenez, F. Moore, J. Spackman, and M. Zondio, "Atmospheric observations of Arctic Ocean methane emissions up to 82° north," Nat. Geosci. **5**, 318–321 (2012).
23. J. Houghton, Y. Ding, D. J. Griggs, M. Noguer, P. J. van der Linden, X. Dai, K. Maskell, and C. A. Johnson, eds., *Climate Change 2001: The Scientific Basis* (Cambridge University, 2001).
24. National Research Council, *Decadal Survey: Earth Science and Applications from Space: National Imperatives for the Next Decade and Beyond* (National Academic, 2007).
25. NASA, "NASA ASCENDS Workshop," http://cce.nasa.gov/ascends_2012/index.html.
26. G. Ehret, A. Fix, C. Kiemle, and A. Wirth, "Space-borne monitoring of methane by intergrated path differential absorption lidar: perspective of DLR's CHARM-SSB mission," *Proceedings of the 24th International Laser Radar Conference* (2008), pp. 1208–1211.
27. C. Stephan, M. Alpers, B. Millet, G. Ehret, P. Flamant, and C. Deniel, "MERLIN: a space-based methane monitor," Proc. SPIE **8159**, 815908 (2011).
28. A. Fix, C. Büdenbender, M. Wirth, M. Quatrevalet, A. Amediek, C. Kiemle, and G. Ehret, "Optical parametric oscillators and amplifiers for airborne and spaceborne active remote sensing of CO_2 and CH_4," [Lidar Technologies, Techniques, and Measurements for Atmospheric Remote Sensing VII, 818206], Proc. SPIE **8182**, 818206 (2011).
29. M. D. Smith, "Spacecraft observations of the Martian atmosphere," Annu. Rev. Earth Planet. Sci. **36**, 191–219 (2008).
30. M. J. Mumma, R. E. Novak, M. A. DiSanti, and B. P. Bonev, "A sensitive search for methane on Mars," Bull. Am. Astron. Soc. **35**, 937–938 (2003).
31. M. J. Mumma, R. E. Novak, M. A. DiSanti, B. P. Bonev, and N. Dello Russo, "Detection and mapping of methane and water on Mars," Bull. Am. Astron. Soc. **36**, 1127 (2004).
32. M. J. Mumma, G. L. Villanueva, R. E. Novak, T. Hewagama, B. P. Bonev, M. A. DiSanti, A. M. Mandell, and M. D. Smith, "Strong release of methane on Mars in northern summer 2003," Science **323**, 1041–1045 (2009).
33. P. H. Smith, L. K. Tamppari, R. E. Arvidson, D. Bass, D. Blaney, W. V. Boynton, A. Carswell, D. C. Catling, B. C. Clark, T. Duck, E. DeJong, D. Fisher, W. Goetz, H. P. Gunnlaugsson, M. H. Hecht, V. Hipkin, J. Hoffman, S. F. Hviid, H. U. Keller, S. P. Kounaves, C. F. Lange, M. T. Lemmon, M. B. Madsen, W. J. Markiewicz, J. Marshall, C. P. McKay, M. T. Mellon, D. W. Ming, R. V. Morris, W. T. Pike, N. Renno, U. Staufer, C. Stoker, P. Taylor, J. A. Whiteway, and A. P. Zent, "H2O at the Phoenix Landing Site," Science **325**, 58 (2009).
34. R. W. Zureka, A. Chicarrob, M. A. Allen, J.-L. Bertaux, R. T. Clancy, F. Daerden, V. Formisano, J. B. Garvin, G. Neukum, and M. D. Smith, "Assessment of a 2016 mission concept: the search for trace gases in the atmosphere of Mars," Planet. Space Sci. **59**, 284–291 (2011).
35. K. Numata, H. Riris, S. Li, S. Wu, S. R. Kawa, M. Krainak, and J. Abshire, "Ground demonstration of a trace gas lidar based on optical parametric amplifiers," J. Appl. Remote Sens. **6**, 063561 (2012).
36. H. Riris, S. Li, K. Numata, S. Wu, J. Burris, A. W. Yu, M. Krainak, and J. B. Abshire, "Methane measurements using optical parametric technology," *American Geophysical Union, Fall Meeting 2009* (American Geophysical Union, 2009), abstract no. A41C-0106.
37. D. G. Murdock, S. V. Stearns, R. T. Lines, D. Lenz, D. M. Brown, and C. R. Philbrick, "Applications of real-world gas detection: airborne natural gas emission lidar (ANGEL) system," J. Appl. Remote Sens. **2**, 023518 (2008).

38. A. Minato, M. A. Joarder, S. Ozawa, M. Kadoya, and N. Sugimoto, "Laser long-path absorption lidar technique for measuring methane using gas correlation method," Jpn. J. Appl. Phys. **38**, 6130–6132 (1999).
39. Y. Kamali, J. F. Daigle, F. Théberge, M. Châteauneuf, A. Azarm, Y. Chen, C. Marceau, Z.-D. Sun, J. Bernhardt, S. C. Lessard, F. Lessard, G. Roy, J. Dubois, and S. L. Chin, "Remote sensing of trace methane using mobile femtosecond laser system of T&T Lab," Opt. Commun. **282**, 2062–2065 (2009).
40. M. J. T. Milton, T. D. Gardiner, T. Molero, and J. Galech, "Injection-seeded optical parametric oscillator for range-resolved DIAL measurements of atmospheric methane," Opt. Commun. **142**, 153–160 (1997).
41. E. R. Crosson, "A cavity ring-down analyzer for measuring atmospheric levels of methane, carbon dioxide, and water vapour," Appl. Phys. B **92**, 403–408 (2008).
42. C. Webster, "Measuring methane and its isotopes $^{12}CH_4$, $^{13}CH_4$, and CH_3D on the surface of Mars with in situ laser spectroscopy," Appl. Opt. **44**, 1226–1235 (2005).
43. S. Wright, G. Duxbury, and N. Langford, "A compact quantum-cascade laser based spectrometer for monitoring the concentrations of methane and nitrous oxide in the troposphere," Appl. Phys. B **85**, 243–249 (2006).
44. L. S. Rothman, I. E. Gordon, A. Barbe, D. C. Benner, P. F. Bernath, M. Birk, V. Boudon, L. R. Brown, A. Campargue, J.-P. Champion, K. Chance, L. H. Coudert, V. Dana, V. M. Devi, S. Fally, J.-M. Flaud, R. R. Gamache, A. Goldman, D. Jacquemart, I. Kleiner, N. Lacome, W. J. Lafferty, J.-Y. Mandin, S. T. Massie, S. N. Mikhailenko, C. E. Miller, N. Moazzen-Ahmadi, O. V. Naumenko, A. V. Nikitin, J. Orphal, V. I. Perevalov, A. Perrin, A. Predoi-Cross, C. P. Rinsland, M. Rotger, M. Šimečková, M. A. H. Smith, K. Sung, S. A. Tashkun, J. Tennyson, R. A. Toth, A. C. Vandaele, and J. Vander Auwera, "The HITRAN 2008 molecular spectroscopic database," J. Quant. Spectrosc. Radiat. Transfer **110**, 533–572 (2009).
45. K. Numata, J. R. Chen, S. T. Wu, J. B. Abshire, and M. A. Krainak, "Frequency stabilization of distributed-feedback laser diodes at 1572 nm for lidar measurements of atmospheric carbon dioxide," Appl. Opt. **50**, 1047 (2011).
46. A. Amediek, A. Fix, M. Wirth, and G. Ehret, "Development of an OPO system at 1.57 μm for integrated path DIAL measurement of atmospheric carbon dioxide," Appl. Phys. B **92**, 295–302 (2008).
47. R. Measures, *Laser Remote Sensing* (John Wiley & Sons, 1984).
48. J. B. Abshire, H. Riris, G. Allan, C. J. Weaver, J. Mao, X. Xiaoli Sun, W. E. Hasselbrack, R. S. Kawa, and S. Biraud, "Pulsed airborne lidar measurements of atmospheric CO_2 column absorption," Tellus **62**, 770–783 (2010).
49. G. Ehret, C. Kiemle, W. Wirth, A. Amediek, A. Fix, and S. Houwling, "Space-borne remote sensing of CO_2, CH_4, and N_2O by integrated path differential absorption lidar: a sensitivity analysis," Appl. Phys. B **90**, 593–608 (2008).
50. S. A. Clough and M. J. Iacono, "Line-by-line calculations of atmospheric fluxes and cooling rates. 2: applications to carbon dioxide, ozone, methane, nitrous oxide, and the halocarbons," J. Geophys. Res. **100**, 16519–16535 (1995).
51. A. Amediek, X. Sun, and J. B. Abshire, "Analysis of column height measurements from a pulsed airborne CO_2 integrated path differential absorption lidar," IEEE Trans. Geosci. Remote Sens. (to be published).
52. Global Modeling and Assimilation Office, http://gmao.gsfc.nasa.gov/.
53. P. Werle, R. Mucke, and F. Slemr, "The limits of signal averaging in atmospheric trace-gas monitoring by tunable diode-laser absorption spectroscopy (TDLAS)," Appl. Phys. B **57**, 131–139 (1993).
54. P. Werle, P. Mazzinghi, F. D'Amato, M. De Rosa, K. Maurer, and F. Slemr, "Signal processing and calibration procedures for in situ diode-laser absorption spectroscopy," Spectrochim. Acta A **60**, 1685–1705 (2004).
55. H. Riris, C. B. Carlisle, R. E. Warren, and D. E. Cooper, "Signal to noise ratio enhancement in frequency modulation spectrometers using digital signal processing," Opt. Lett. **19**, 144 (1994).
56. D. S. Bomse and D. J. Kane, "An adaptive singular value decomposition (SVD) algorithm for analysis of wavelength modulation spectra," Appl. Phys. B **85**, 461–466 (2006).